Temperature evolution of interferometer visibility in a small radius fibre coil current sensor

S.K. Morshnev, V.P. Gubin, N.I. Starostin, Ya.V. Przhiyalkovsky, A.I. Sazonov

Abstract. **We have experimentally demonstrated periodic oscillations of interferometer visibility in a current sensor in response to changes in the temperature of a small-radius spun fibre sensing coil. The observed effect has been shown to depend on the magnitude of the bend-induced linear birefringence in the spun fibre in the magnetically sensitive coil and the temperature behaviour of the built-in linear birefringence in the fibre. Using a model that considers a helical structure of the built-in linear birefringence axes in spun fibre, we have shown that the above factors result in periodic oscillations of the ellipticity of polarised light at the ends of the sensing coil and that this underlies the temperature oscillations of interferometer visibility in the current sensor. The effect may cause errors in the response of a fibre-optic current sensor with a small sensing coil.**

1. Introduction

Faraday effect fibre-optic current sensing [1–4] requires the use of a sensitive interferometric scheme with equal optical paths for interfering waves [5]. For this purpose, use is most often made of a linear reflective interferometer configuration [6] (e.g. Rayleigh interferometer), where the waves exchange their optical paths when travelling backwards, which makes it possible to compensate for the considerable phase shift they acquire while travelling in the forward direction and ensures interference between them with zero path difference in a wide wavelength range. The phase difference due to the Faraday effect then doubles, rather than being compensated [1, 4, 6], because of the vector character of the magnetic field. As a sensing coil wound around a conductor carrying the electric current to be measured, one commonly uses a spun-fibre coil [2, 4]. It is known [7–9] that spun fibre does not maintain the circular polarisation state of propagating waves, but can maintain the rotation direction of the electric field vector of elliptically polarised waves, thereby ensuring Faraday phase shift accumulation over the length of the spun fibre [4].

S.K. Morshnev, V.P. Gubin, N.I. Starostin, Ya.V. Przhiyalkovsky, A.I. Sazonov V.A. Kotel'nikov Institute of Radio Engineering and Electronics (Fryazino Branch), Russian Academy of Sciences, pl. Vvedenskogo 1, 141190 Fryazino, Moscow region, Russia; e-mail: nis229@ire216.msk.su

In a number of applications, it is necessary to use small-radius sensing coils, in particular, if there is a limited space for a sensing element. At a small fibre bend radius R, linear birefringence (BR) is induced in the fibre, with a beat length L_{ind} proportional to R^2. This reduces the magneto-optical sensitivity of the fibre coil [2, 4, 8, 9] (which can generally be compensated for by increasing the number of turns in the coil) and interferometer visibility [10, 11], thereby degrading the threshold sensitivity of the current sensor and, accordingly, reducing the dynamic range of measurable currents. These changes are due to the decrease in light ellipticity in spun fibre [10, 11]. The effect of parameters of spun fibre and fibre bend radius on interferometer visibility has been the subject of a number of studies [10, 11], where approaches were proposed for improving visibility at low light ellipticity in fibre. Gubin et al. [4] and Polinkin and Blake [12] detected spatial variations in magneto-optical sensitivity along the length of the fibre in a small-radius coil. Here we report observation of variations in the visibility of a reflective interferometer in a current sensor in response to changes in the temperature of a small-radius sensing coil. The purpose of this work is to understand the physical mechanism underlying these variations.

2. Experimental

Figure 1 shows a schematic of the experimental setup, which has the form of a reciprocal reflective interferometer. Light from a fibre-optic superluminescent source (*1*) with an inhomogeneous bandwidth of ~20 nm passes through a coupler (*2*) and linear polariser (*3*) and excites two orthogonal linearly polarised waves identical in intensity in hi-bi fibre for each spectral component. This is ensured by a fusion splice (*6*) made so that the polariser axes are oriented at 45° with respect to the BR axes of the hi-bi fibre at the input of a piezoceramic fibre modulator (*4*), which introduces a phase differ-
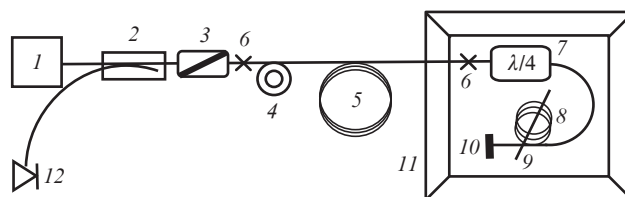

Figure 1. Optical layout of the experimental setup: (*1*) erbium-doped fibre superluminescent source; (*2*) fibre coupler; (*3*) fibre polariser; (*4*) piezoceramic phase modulator; (*5*) hi-bi fibre delay line; (*6*) 45° splice; (*7*) fibre quarter-wave plate; (*8*) spun-fibre coil; (*9*) current-carrying conductor; (*10*) mirror; (*11*) thermal chamber; (*12*) photodetector.

ence $\Phi = \Phi_0 \cos\omega t$ between the waves. The waves then propagate through an ~1200-m phase delay line (5), also made of hi-bi fibre. During the propagation through a given hi-bi fibre segment, the wave polarised along the slow axis X (X wave) acquires a larger phase shift than does the wave polarised along the fast axis Y (Y wave). As a result, at the output of the long delay line (5) the waves are incoherent.

Passing through the fusion splice (6) and quarter-wave plate (7), the waves become circularly polarised: for example, the X wave becomes a right-hand circularly polarised (R) wave and the Y wave becomes a left-hand circularly polarised (L) wave. The waves then propagate in the form of elliptical waves, $\mathcal{E}_{XR}$ and $\mathcal{E}_{YL}$, through the spun fibre wound in the form of a coil (8), retaining their original rotation directions. In the case of a large-radius coil, the waves are nearly circularly polarised: $\mathcal{E}_{XR}$ is similar to C_{XR}, and $\mathcal{E}_{YL}$, to C_{YL}. The phase difference between the waves continues to increase. The phases of the C_{XR} and C_{YL} waves reach φ_1 and φ_2, respectively (with $\varphi_1 \gg \varphi_2$), when the waves arrive at the mirror (10). The waves remain incoherent. The phase difference is also contributed by the phase difference resulting from the Faraday effect due to the magnetic field generated by the current that passes through a copper conductor (solenoid) (9) and should be measured. The mirror (10) transforms the circularly polarised waves: the left-hand wave becomes right-hand polarised ($C_{YL} \rightarrow C_{YLR}$) and the right-hand wave becomes left-hand polarised ($C_{XR} \rightarrow C_{XRL}$). The subscripts used here specify the starting wave as well.

Since the rotation direction of the helical structure of spun fibre is independent of the light propagation direction, the phase difference between orthogonally polarised waves, due to reciprocal effects, decreases during backward propagation of the waves through the spun fibre, whereas the Faraday effect-induced phase difference increases because of the vector character of the magnetic field (the Faraday effect-induced phase difference between the waves changes sign, depending on their propagation direction: along the field or in the opposite direction). Passing through the quarter-wave plate (7) in the backward direction, the right-hand polarised wave transforms into an X wave ($C_{YLR} \rightarrow X_{YLR}$), and the left-hand polarised wave, into a Y wave ($C_{XRL} \rightarrow Y_{XRL}$). Here the subscripts indicate that the starting Y wave transformed into an X wave and the starting X wave transformed into a Y wave. Thus, after backward propagation the two waves will have identical phase shifts ($\varphi_1 + \varphi_2$), will become coherent and, after passing through a polariser (3) and coupler (2), will be able to interfere at a photodetector (12).

In our experiments, the same segment of spun fibre, of length $L_f = 4.83$ m, was used to produce magnetically sensitive coils. We investigated two magnetically sensitive coils. Coil A consisted of eight 95-mm-radius turns of fibre in the form of a free coil in a quartz tube placed in a solenoid consisting of 1100 turns of 1-mm-diameter copper wire, through which a current of 2 A was passed. Coil B consisted of 56 14-mm-radius turns of spun fibre wound onto a cardboard tube. The coil was surrounded by 66 turns of 1-mm-diameter copper wire, through which a current of 2 A was passed.

The power dissipated in the copper windings was insignificant: 1.28 and 0.06 W for coils A and B, respectively. The spun fibre cleave served as a Fresnel reflector (10). The quarter-wave plate, 1.7 mm long, was made of hi-bi fibre with a reduced temperature coefficient of BR (~10^{-5} K^{-1}). The magnetically sensitive coil (8), copper solenoid (9), mirror (10) and quarter-wave plate (7) were enclosed in a thermal chamber, in which the temperature was maintained with a stability of ± 0.1°C. The temperature in the chamber was varied at a rate of 30°C h^{-1}. At this temperature scan rate, the heat capacity of the coil (together with the copper solenoid) did not slow the response of the coil to temperature changes in the chamber.

Interference visibility was evaluated in real time from two components of the modulation signal: constant component and second harmonic of the modulation frequency. Temperature dependences of the measured fringe visibility are presented in Fig. 2a for coil A and Fig. 2b for coil B. The coils are seen to differ significantly in the behaviour of visibility. In the case of coil A, visibility varies little with temperature, whereas the temperature dependence of visibility for coil B has the form of harmonic oscillations with a period $\Delta T \approx 34$°C and amplitude of ~8% of the peak visibility. To interpret these dependences, we employ the model described in the next section.
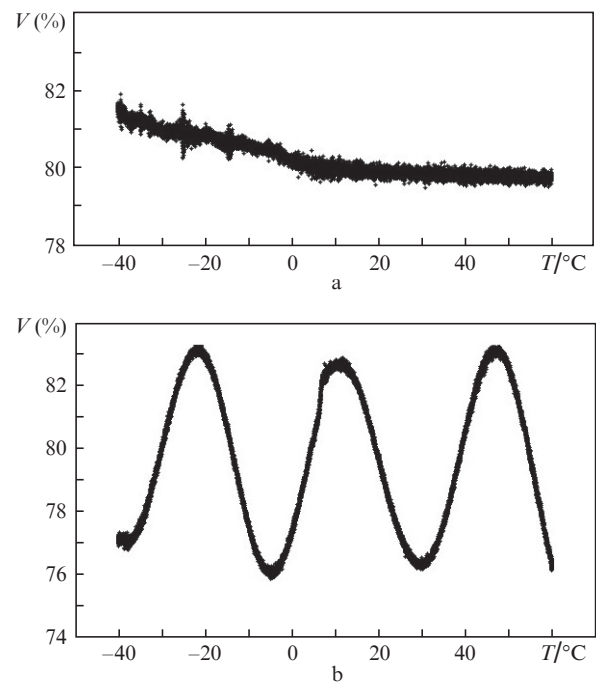

Figure 2. Experimentally determined interference visibility V as a function of temperature T at (a) a large ($R = 95$ mm) and (b) a small ($R = 14$ mm) winding radius.

3. Theory

3.1. Interference of light waves in a reflective interferometer with a magnetically sensitive spun-fibre coil

Light propagating through spun fibre is in general elliptically polarised [4, 9, 10]. Consider how the ellipticity acquired by the wave in the magnetically sensitive spun-fibre coil influences interference visibility. In a linear polarisation basis, the Jones vector of an elliptically polarised wave can be written in the most general form [13]:

$$\begin{vmatrix} E_X \\ E_Y \end{vmatrix} = \begin{vmatrix} \cos\theta\cos\varepsilon - \mathrm{i}\sin\theta\sin\varepsilon \\ \sin\theta\cos\varepsilon + \mathrm{i}\cos\theta\sin\varepsilon \end{vmatrix} \sqrt{\frac{I}{2}}, \qquad (1)$$

where θ is the azimuth angle of the polarisation ellipse; $\varepsilon = \arctan(b/a)$ is the ellipticity angle; b and a are the minor and major axes of the polarisation ellipse; and I is the intensity of the wave. At two points in the optical path considered above [when the wave is reflected from the mirror (*10*) and when it passes through the quarter-wave plate (*7*) in the backward direction], the initial polarisation state of the wave – circularly or elliptically polarised – is important. At the former point, a circularly polarised wave does not change its rotation direction during propagation through the coil in the forward direction and, after reflection from the mirror, has a circular polarisation orthogonal to the initial one. At the latter point, the circularly polarised wave transforms into a linearly polarised one.

All is not so simple if the initial polarisation state is elliptical. The Jones vector (1) can be represented in a circular polarisation basis. In the case of an elliptically polarised wave, this means the decomposition into two orthogonal, right and left circularly polarised waves [13]:

$$\begin{vmatrix} E_R \\ E_L \end{vmatrix} = \begin{vmatrix} E_X \\ E_Y \end{vmatrix} \begin{Vmatrix} 1 & -i \\ 1 & i \end{Vmatrix}. \tag{2}$$

Substituting (1) into (2) we obtain

$$\begin{vmatrix} E_R \\ E_L \end{vmatrix} = \begin{vmatrix} (\cos\varepsilon + \sin\varepsilon)\exp(-i\theta) \\ (\cos\varepsilon - \sin\varepsilon)\exp(i\theta) \end{vmatrix} \sqrt{\frac{I}{2}}. \tag{3}$$

It is seen that any elliptical polarisation state ($|\varepsilon| < 45°$) engenders two orthogonal circularly polarised waves, C_J^R and C_J^L, where the subscript J refers to the elliptically polarised starting wave $\mathcal{E}_J$ with the right ($J = R$) or left ($J = L$) rotation direction. While propagating through spun fibre, the orthogonal circularly polarised starting waves transform into elliptically polarised waves having identical ellipticity angles, $|\varepsilon|$, which differ only in sign [4, 7–9].

A circularly polarised wave is formed by the quarter-wave plate (*7*) from a linearly polarised wave having an electric field vector parallel to the slow or fast axis of the hi-bi fibre in the delay line (*5*) (Fig. 1). As a result, when approaching the mirror the right and left hand elliptically polarised waves have total phase delays (between the polariser and mirror) φ_1 and φ_2, respectively. As mentioned in Section 2, $\varphi_1 \gg \varphi_2$ and the waves are incoherent. After reflection from the mirror, they experience polarisation conversion: the right-hand wave becomes left-hand polarised and the left-hand wave becomes right-hand polarised. Let Γ_R be the amplitude of the right hand elliptically polarised wave $\mathcal{E}_R$, and let E_R^R and E_R^L be the amplitudes of the right and left hand circularly polarised waves C_R^R and C_R^L which result from the decomposition of the $\mathcal{E}_R$ wave. After reflection from the mirror, the C_R^R wave becomes a left-hand polarised wave, C_{RL}, of amplitude E_{RL}, and the C_R^L wave becomes a right-hand polarised wave, C_{RR}, of amplitude E_{RR}. Similarly, let Γ_L be the amplitude of the left hand elliptically polarised wave $\mathcal{E}_L$, and let E_L^R and E_L^L be the amplitudes of the right and left hand circularly polarised waves C_L^R and C_L^L which result from the decomposition of the $\mathcal{E}_L$ wave. After reflection from the mirror, the right-hand polarised wave C_L^R becomes a left-hand polarised wave, C_{LL}, of amplitude E_{LL}, and the left-hand polarised wave C_L^L becomes a right-hand circularly polarised wave, C_{LR}, of amplitude E_{LR}.

Passing through the quarter-wave plate in the backward direction, the C_{RR} and C_{LR} waves become linearly polarised along the X axis and the C_{RL} and C_{LL} waves become linearly polarised along the Y axis of the hi-bi fibre in the delay line, i.e. propagating in the backward direction (through the spun fibre and delay line), the C_{RR} and C_{LR} waves acquire a phase shift φ_1, as the right hand polarised component above, and the C_{RL} and C_{LL} waves acquire a phase shift φ_2. The total phase shifts $\Delta\varphi$ are as follows: $2\varphi_1$ for the C_{RR} wave, $\varphi_1 + \varphi_2$ for the C_{RL} wave, $\varphi_2 + \varphi_1$ for the C_{RL} wave and $2\varphi_2$ for the C_{LL} wave. Taking into account the nonreciprocal phase shift 2Φ between the starting waves $\mathcal{E}_L$ and $\mathcal{E}_R$ due to the Faraday effect and modulation, we can describe the four waves as follows:

$$\Gamma_R \rightarrow$$

$$\begin{cases} E_R^R \rightarrow E_{RL} = \dfrac{\sqrt{I_0}}{2}(\cos\varepsilon + \sin\varepsilon)\exp[i(\omega t + \varphi_1 + \varphi_2 - \theta + \Phi)], \\ E_R^L \rightarrow E_{RR} = \dfrac{\sqrt{I_0}}{2}(\cos\varepsilon - \sin\varepsilon)\exp[i(\omega t + 2\varphi_1 + \theta + \Phi)], \end{cases}$$

$$\Gamma_L \rightarrow \tag{4}$$

$$\begin{cases} E_L^R \rightarrow E_{LL} = \dfrac{\sqrt{I_0}}{2}(\cos\varepsilon - \sin\varepsilon)\exp[i(\omega t + 2\varphi_2 + \theta - \Phi)], \\ E_L^L \rightarrow E_{LR} = \dfrac{\sqrt{I_0}}{2}(\cos\varepsilon + \sin\varepsilon)\exp[i(\omega t + \varphi_1 + \varphi_2 - \theta - \Phi)]. \end{cases}$$

It is worth noting that only the components having identical phase shifts, $\Delta\varphi = \varphi_1 + \varphi_2$, can interfere. The other components are incoherent and contribute only to the background of the interference pattern. After passing through the analyser, the orthogonal components can interfere. The intensity of the light at the detector input is

$$\langle I \rangle = \frac{1}{2}(E_{RL} + E_{RR} + E_{LR} + E_{LL})(E_{RL}^* + E_{RR}^* + E_{LR}^* + E_{LL}^*). \tag{5}$$

The interference conditions are such that there are only six nonzero terms on the right-hand side of (5) and it takes the form

$$\langle I \rangle = \frac{1}{2}(E_{LR}E_{LR}^* + E_{LR}E_{RL}^* + E_{RR}E_{RR}^*$$
$$+ E_{RL}E_{LR}^* + E_{RL}E_{RL}^* + E_{LL}E_{LL}^*). \tag{6}$$

Substituting relevant expressions from (4) into (6), we obtain

$$\langle I \rangle = \frac{I_0}{8}[2(\cos\varepsilon + \sin\varepsilon)^2 + 2(\cos\varepsilon - \sin\varepsilon)^2 + 2(\cos\varepsilon + \sin\varepsilon)^2$$
$$\times \cos 2\Phi] = \frac{I_0}{2}\left[1 + \frac{(\cos\varepsilon + \sin\varepsilon)^2}{2}\cos 2\Phi\right]. \tag{7}$$

Therefore, visibility is given by

$$V = \frac{I_{max} - I_{min}}{I_{max} + I_{min}} = \frac{(\cos\varepsilon + \sin\varepsilon)^2}{2}. \tag{8}$$

Thus, the smaller is the ellipticity angle ε of an elliptically polarised wave in front of the mirror, the lower is the interference fringe contrast. Similar results can be obtained for another case: an elliptical polarisation state (PS) of the light at the output of the coil [in front of the quarter-wave plate (*7*) during backward propagation].

3.2. Evolution of the PS along spun fibre at a large coil radius

As shown earlier [4, 7–9], in a model that considers a helical structure of the built-in linear BR axes for spun fibre with a bend radius R, placed in a magnetic field longitudinal with respect to the fibre axis, we obtain the following expression in a linear polarisation basis [8, 9]:

$$\begin{Vmatrix} dE_X/dz \\ dE_Y/dz \end{Vmatrix} = \frac{1}{2}$$

$$\times \begin{Vmatrix} i[\Delta\beta\cos 2\xi z + \delta\cos 2\varphi_0] & -\gamma + i[\Delta\beta\sin 2\xi z + \delta\sin 2\varphi_0] \\ \gamma + i[\Delta\beta\sin 2\xi z + \delta\sin 2\varphi_0] & -i[\Delta\beta\cos 2\xi z + \delta\cos 2\varphi_0] \end{Vmatrix}$$

$$\times \begin{Vmatrix} E_X \\ E_Y \end{Vmatrix}, \tag{9}$$

where E_X and E_Y are the components of the optical field; $\Delta\beta = 2\pi/L_b$ is the phase delay per unit length between linearly polarised modes; L_b is the built-in linear BR beat length in the spun fibre; $\xi = 2\pi/L_{tw}$ is the rotation rate of the axes per unit length along the helical structure; L_{tw} is the spin pitch; γ is the external magnetic field-induced phase delay per unit length between circularly polarised modes; $\delta = 2\pi/L_{ind}$ is the phase delay per unit length between linearly polarised modes due to a spun fibre bend of radius R; φ_0 is the angle between the linear polarisation vector and the X axis of the helical structure; and z is a coordinate along the fibre axis.

The beat length of the bend-induced linear BR, L_{ind}, is given by [14]

$$L_{ind} = \frac{4\pi}{C_s}\frac{R^2}{r^2}. \tag{10}$$

Here r is the outer fibre radius and the coefficient C_s is given by [14]

$$C_s = 0.5k_0 n_0^3 (p_{11} - p_{12})(1 - v_P), \tag{11}$$

where k_0 is the magnitude of the wave vector; n_0 is the average refractive index of the fibre; p_{11} and p_{12} are components of the elasto-optic tensor of the fibre material; and v_P is Poisson's ratio. For a 125-µm-diameter silica fibre at a wavelength $\lambda = 1550$ nm, formula (10) has the form $L_{ind} \approx (3/1\text{ mm})R^2$.

Figure 3 illustrates the evolution of the PS on the Poincare sphere, where the latitude of a point is twice the ellipticity angle and its longitude is twice the azimuth angle of the PS. The northern hemisphere contains all right-hand polarisation states and the southern hemisphere contains all left-hand states. The equator is occupied by all linearly polarised states. The north pole corresponds to right-hand circularly polarised states, and the south pole, to left-hand circularly polarised states. The results were obtained by numerically solving Eqn (9) [4, 8, 9]. The evolution of the PS in Fig. 3 corresponds to a right-hand circularly polarised initial state in a rectilinear spun fibre ($\delta = 0$, $L_b = 12$ mm). For PS evolution loops not to overlap, the spin pitch L_{tw} was taken to be 6 mm, i.e. twice the standard spin pitch $L_{tw} = 3$ mm. It is seen in Fig. 3 that the PS's of a propagating wave participate in two types of motion: 'fast', which we refer to as nutation, by analogy with the motion of a gyroscope, and 'slow', referred to as precession.

After completing a precession loop, the PS returns to its original position. In Fig. 3 ($L_b = 12$ mm), in the case of nutation one loop corresponds to light propagation over $l = 3$ mm, i.e. over half the spin pitch, whereas a precession loop reaches completion at $l = 96$ mm. For the standard spin pitch $L_{tw} = 3$ mm, nutation and precession loops reach completion at $l = 1.5$ and 183 mm, respectively.
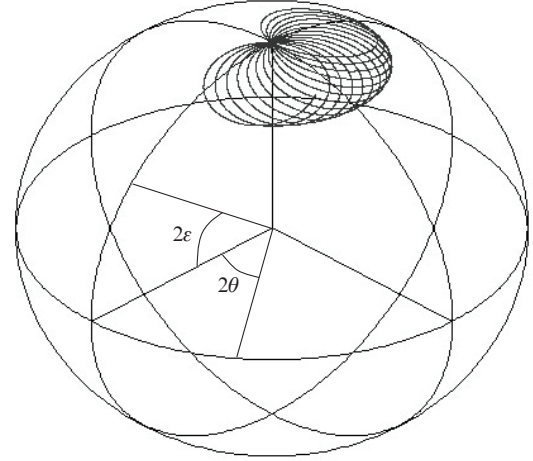

Figure 3. Evolution of the PS on the Poincare sphere for a right-hand circularly polarised wave in a rectilinear spun fibre. The latitude of a point is twice the ellipticity angle, 2ε, and its longitude is twice the azimuth angle, 2θ. Parameters of the fibre: $L_b = 12$ mm and $L_{tw} = 6$ mm.

A spun fibre bend with the standard parameters indicated above when it is coiled with a large radius [$\delta \ll \Delta\beta$ up to $R \approx 25$ mm ($L_{ind} = 1875$ mm $\gg L_b = 12$ mm)] has no effect on the nature of the precession – motion of the PS around the pole with a deviation within 41°. Not only do polarisation states retain their rotation direction, but they are also similar to a circularly polarised state ($\varepsilon_{av} > 41°$). Moreover, we use a broadband light source and, as shown earlier [15], nutation motions are averaged over the wavelength to give the average value ε_{av}. Estimation by formula (8) at $\varepsilon_{av} > 41°$ yields $V = 0.99$. Thus, at large coil radii ($R \gg 25$ mm) the effect that the PS ellipticity on the mirror and at the coil output (during backward propagation) has on interferometer visibility can be neglected.

3.3. Evolution of the PS of waves along spun fibre at a small coil radius

The nature of the PS evolution at small bend radii ($R < 25$ mm) differs significantly from that above. In this case, precession occurs not around the pole of the Poincare sphere but around a vector determined by the bend radius [8, 9, 14]. Figure 4a illustrates the evolution of the PS in spun fibre with parameters that are used below: built-in BR beat length $L_b = 12$ mm, spin pitch $L_{tw} = 3$ mm, bend radius $R = 14$ mm, bend-induced BR beat length $L_{ind} = 588$ mm and fibre segment length $L_f = 150$ mm. The precession length L_{pr} corresponding to a closed cycle is 183 mm. It is seen that the precession radius considerably exceeds the nutation radii, so PS's may have small ellipticity angles (compared to the ellipticity angle at the initial precession point) and averaging over the spectrum of the broadband light source will not here give similar ε_{av} average values over an entire precession cycle. Figure 4b

presents the ε_1 and ε_2 components of the average ellipticity angle $\varepsilon_{av} = (\varepsilon_1 + \varepsilon_2)/2$ and the maximum (ε_{max}) and minimum (ε_{min}) average angles, which are used in what follows. It is seen in Fig. 5 that $\varepsilon_{av}(L_f/L_{pr})$ depends on what fraction of the precession length L_{pr} is passed in the spun fibre and that the ellipticity angle varies in the range $\varepsilon_{min} \leqslant \varepsilon_{av}(L_f/L_{pr}) \leqslant \varepsilon_{max}$. Note that ε_{min} is reached at $L_f/L_{pr} = N + 1/2$ and ε_{max} is reached at $L_f/L_{pr} = N$, where N is an integer.

Figure 5. Ellipticity angles ε_1, ε_2, ε_{av} of the PS against the fibre length Lf normalised to the precession length L_f ($L_f < L_{pr}$) and the function $F(L_f/L_{pr})$ (see text).

14 mm, the ellipticity angle can be substantially smaller than 45°, i.e. it can experience considerable oscillations. In the case under consideration, the ellipticity angle is $\varepsilon_{min} = 23°$, which reduces fringe visibility (8) to 0.74 (with allowance for the mirror and $\lambda/4$ plate).

3.4. Temperature dependence of the precession length

The precession length L_{pr} depends on the spin pitch L_{tw} of the helical structure of the built-in BR axes in the spun fibre and the built-in BR beat length L_b. The beat length L_b depends on temperature T (see e.g. Refs [16, 17]): $L_b(T) = L_{b0}[1 + \alpha(T - T_0)]$, where in our case $L_{b0} = 12$ mm, $T_0 = 0$ °C and $\alpha = 7 \times 10^{-4}$ K^{-1}. The temperature dependence of the spin pitch L_{tw} for silica fibres is weak compared to that of the beat length and can be neglected.

To calculate the precession length L_{pr} as a function of temperature T, we used only fibre lengths that were multiples of the nutation period and led to a circular PS coinciding with the initial state. The calculation results are presented in Fig. 6. It is seen that the relation is linear:

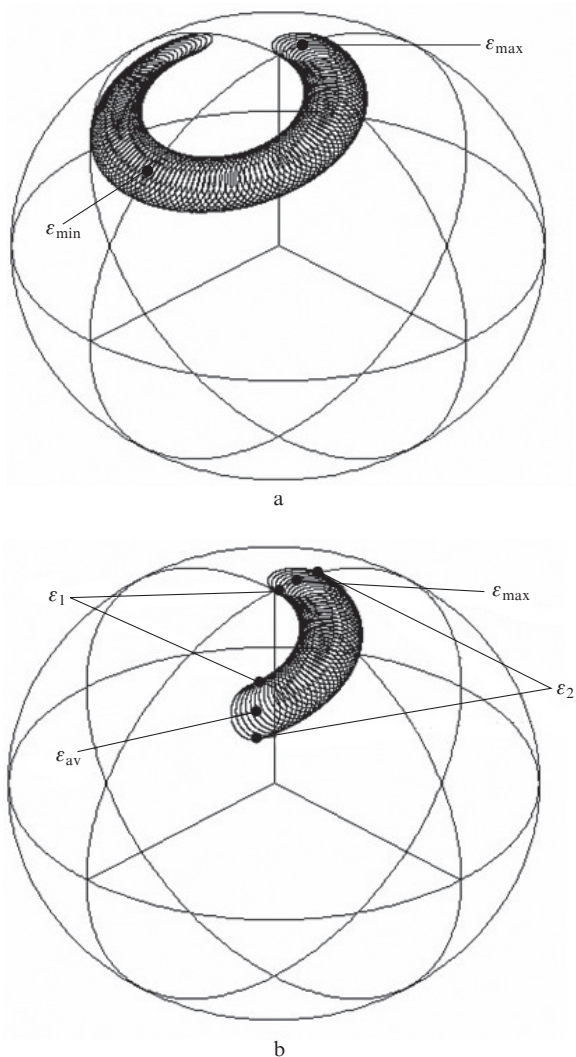$$L_{pr} = L_{pr0}[1 + \alpha_1(T - T_0)], \qquad (13)$$

Figure 4. Evolution of the PS on the Poincare sphere at $R = 14$ mm ($L_{ind} = 588$ mm) for spun fibre with $L_f =$ (a) 150 and (b) 60 mm. The dots indicate the coordinates of calculated ε_1, ε_2, ε_{av}, ε_{max} and ε_{min}. Parameters of the spun fibre: $L_{tw} = 3$ mm and $L_b = 12$ mm.

We calculated ε_1 and ε_2 as functions of L_f/L_{pr} in the range $0 \leqslant L_f \leqslant L_{pr}$ and $\varepsilon_{av}(L_f/L_{pr})$. The results are presented in Fig. 5. An attempt to represent $\varepsilon_{av}(L_f/L_{pr})$ as the function

$$F\left(\frac{L_f}{L_{pr}}\right) = \frac{\varepsilon_{max} + \varepsilon_{min}}{2} + \frac{\varepsilon_{max} - \varepsilon_{min}}{2} \cos\left(2\pi \frac{L_f}{L_{pr}}\right) \qquad (12)$$

was only partially successful (solid line in Fig. 5): this function adequately describes the position of ε_{max} and ε_{min} (data points in Fig. 5). This allowed us to use it subsequently for initially determining the parameters in question and their position. The main conclusion from the data in Fig. 5 is that, at $R =$
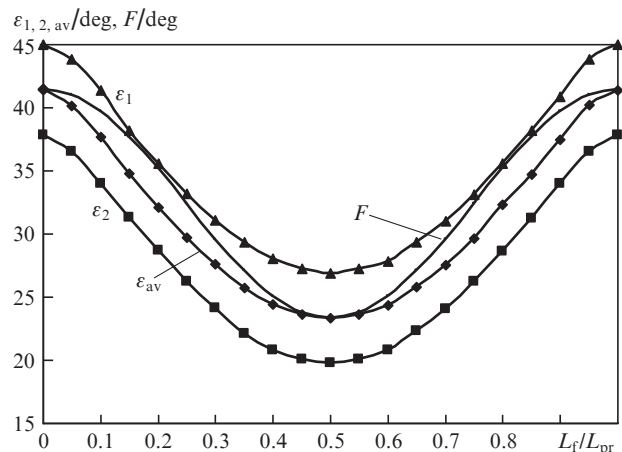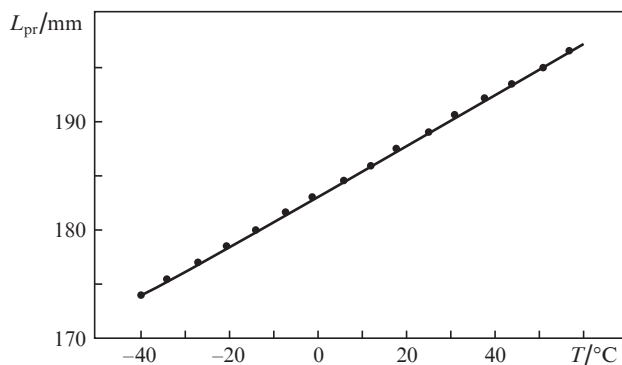

Figure 6. Calculated precession length L_{pr} as a function of temperature T.

with $\alpha_1 = 0.00127$ K^{-1} and $L_{pr0} = 183$ mm. At beat lengths in the range 11 mm $< L_b <$ 13 mm, α_1 remains unchanged.

3.5. Visibility evolution at a varying precession length

The magnetically sensitive coil is made of spun fibre of constant length L_f. The thermal expansion coefficient of silica is $\alpha_{sil} = 4 \times 10^{-6}$ K^{-1}, so in a temperature interval of $\sim 100\,°C$ the length L_f can be taken to be constant, whereas the precession length L_{pr} varies noticeably with temperature ($\alpha_1 = 0.00127$ K^{-1}). Spun fibre of length L_f can be represented as the sum of N segments of length L_{pr} and a segment of length L_{res} ($L_{res} < L_{pr}$):

$$L_f = NL_{pr} + L_{res}. \tag{14}$$

At the coil input, a circularly polarised wave is formed. After passing N complete precession cycles (length NL_{pr}), its PS is again circularly polarised. The wave can become elliptically polarised only in the rest of the fibre, of length L_{res}. From Fig. 5 (after $L_f \rightarrow L_{res}$ substitution), it is easy to find the ellipticity angle $\varepsilon(L_{res}/L_{pr})$ of the wave at the output end of the spun fibre. Variations in the temperature of the coil will lead to changes in the precession length [see relation (13)] and the length of the rest of the fibre (L_{res}), thus changing the ellipticity angle at the coil output. Some idea of this model can be provided by function (12), which adequately describes the period and maximum and minimum values of ε and their position as a function of L_{res}/L_{pr}. Substituting L_{pr} from (13) into (12), we obtain

$$F(L_f/L_{pr}) = \frac{\varepsilon_{max} + \varepsilon_{min}}{2} + \frac{\varepsilon_{max} - \varepsilon_{min}}{2}$$
$$\times \cos\left\{2\pi \frac{L_f}{L_{pr0}[1 + \alpha_1(T - T_0)]}\right\}. \tag{15}$$

It is seen that the ellipticity angle is a periodic function of temperature. The period of this function, ΔT, can be found from the relations

$$\frac{L_f}{L_{pr0}[1 + \alpha_1(T_1 - T_0)]} = N,$$
$$\frac{L_f}{L_{pr0}[1 + \alpha_1(T_2 - T_0)]} = N - 1, \tag{16}$$

$$\Delta T = T_2 - T_1 = \frac{L_{pr0}}{\alpha_1 L_f}. \tag{17}$$

One possible cause of the periodic oscillations in interferometer visibility in response to changes in the temperature of the coil is that the ellipticity of the wave before reflection from the mirror or transformation in the quarter-wave plate varies with temperature. The variation in ellipticity is in general due to the noninteger number of precession lengths corresponding to the length of the spun fibre at a given temperature.

3.6. Nonideality of the quarter-wave plate

The quarter-wave plate (7) (Fig. 1), which produces circularly polarised waves, is made of hi-bi fibre with a small temperature coefficient of BR ($\alpha \approx 10^{-5}$ K^{-1}, temperature-compensated fibre). As indicated above, this plate was fusion-spliced to the output of the hi-bi fibre-based delay line in an appropriate orientation. A deviation of the angle between the axis of the quarter-wave plate and the BR axis in the delay line from 45° in the course of splicing might lead to a marked reduction in ε_{in} at the input of the magnetically sensitive coil [17]. Figure 7 shows calculated ε_{av} at the output end of the spun fibre as a function of L_{res}/L_{pr} at different ε_{in} angles at its input end. It is seen that, with decreasing ε_{in}, the difference $\varepsilon_{max} - \varepsilon_{min}$ first decreases, down to zero at $\varepsilon_{in} = 32.4°$, and then rises, but here ε_{av} reaches a maximum at $L_{res} = {}^1\!/_2 L_{pr}$, rather than at the boundaries of an interval of length L_{pr}, in contrast to what was described above (Fig. 5). Similar results may be due to uncertainty in the length of the quarter-wave plate [17].
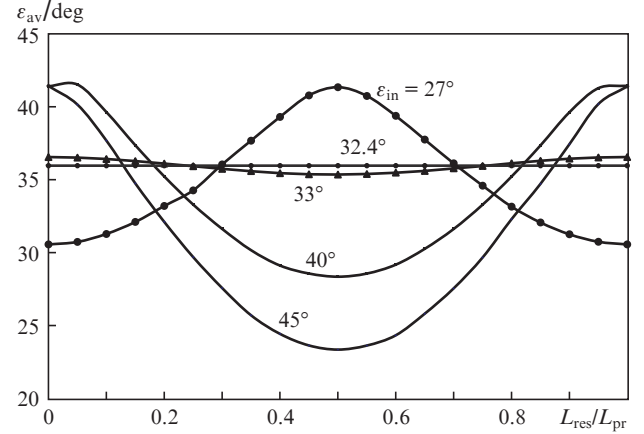
Figure 7. Calculated ellipticity angle ε_{av} at the output end of the spun fibre as a function of L_{res} normalised to the precession length at different input ellipticity angles, ε_{in}.

3.7. Temperature dependence of visibility

To explain in detail the observed temperature dependence of visibility (Fig. 2b), we should find such values of the precession period $L_{pr}(T)$ at which theoretical and experimental visibility functions will be identical in period, 'temperature phase' and amplitude (we use quotation marks to distinguish the 'temperature phase' of the visibility function from the phase of an optical wave). First, using relations (15) and (17) we found $L_{pr0} = 207$ mm and $\alpha_1 = 0.00127$ K^{-1}. Next, we performed exact calculations as follows: Using the temperature T from (15), we found the precession length $L_{pr}(T)$ and, taking into account the total fibre length $L_f = 4.83$ m, calculated the length $L_{res}(T)$ at the same temperature by formula (14). Then we used a PS evolution programme with the following parameters: $L_{tw} = 3$ mm, $L_{ind} = 588$ mm, $L_b(T) = L_{b0}[1 + \alpha(T - T_0)]$ (where $L_{b0} = 12.85$ mm and $\alpha = 7 \times 10^{-4}$ K^{-1}) and $L_{res}(T)$. The input wave was circularly polarised ($\varepsilon_{in} = 45°$). Varying L_{res} in the range 0–0.75 mm, we obtained the maximum and minimum values of ε_1 and ε_2 and took the average [$\varepsilon_{av} = (\varepsilon_1 + \varepsilon_2)/2$, see Fig. 3]. In Section 3.1, we indicated two points in the optical path [in front of the mirror (point 1) and in front of the $\lambda/4$ plate during backward propagation (point 2)] where a deviation of the PS from a circularly polarised state ($|\varepsilon| < 45°$) might reduce fringe visibility. Let visibility factors due to the ellipticity of the wave at points 1 and 2 be denoted as V_1 and V_2 ($V_1 = V_2$). The other causes of the reduction in visibility are represented by an instrumental term, V_{ap}. Then finally we have

$$V = V_1 V_2 V_{ap}. \tag{18}$$

Substituting ε_{av} into (8), we find the visibility factor V_1. The calculation results and experimental data are presented in Fig. 8. The experimental visibility values were obtained by sampling the results presented in Fig. 2b. The solid lines in Fig. 8 represent the calculation results at $V_{ap} = 86\%$. It is seen that the period and 'temperature phase' of the oscillations correspond to the experimental picture, whereas the 'theoretical' oscillation amplitude at $\varepsilon_{in} = 45°$ is more than twice the 'experimental' one.

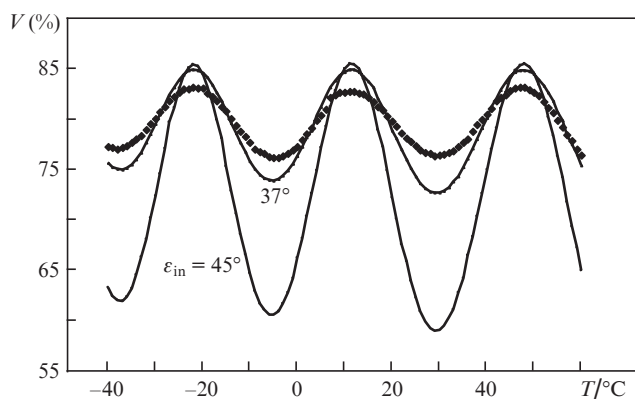**Figure 8.** Experimental (data points) and theoretical (solid lines) visibility functions at different ellipticity angles, ε_{in}.

To account for the decrease in the oscillation amplitude of visibility $V(T)$ by imperfections of the $\lambda/4$ plate, we repeated the exact calculation for an elliptically polarised wave with an input ellipticity angle $\varepsilon_{in} = 37°$. The results are presented in Fig. 8. It is seen that the oscillation amplitude in the theoretical curve became comparable to the amplitude of the experimental curve. The reduction in the oscillation amplitude can be accounted for by the elliptical polarisation of the wave at the input. Reducing the ellipticity angle ε_{in} to $35°$, we obtained perfect agreement in 'temperature phase', period and amplitude between the theoretical and experimental visibility curves. The following parameters of the spun fibre were used in our calculations: $L_{b0} = 12.85$ mm, $\alpha = 7 \times 10^{-4}$ K^{-1}, $L_{tw} = 3$ mm, $L_{pr0} = 207$ mm, $\alpha_1 = 0.00127$ K^{-1}, $R = 14$ mm and $V_{ap} = 85.5\%$.

4. Discussion

As follows from the results presented in section 3.1, the visibility of a reflective interferometer is determined by the ellipticity angle of light at the ends of its sensing coil (in front of the mirror and at the output of the coil). The representation of polarisation evolution analysis results on the Poincare sphere for light propagating through spun fibre (Sections 3.2 and 3.3) demonstrates that, at a small coil radius ($R = 14$ mm), the propagation of a wave through spun fibre is accompanied by PS evolution along a circumference (precession loop) on a Poincare sphere with a centre displaced from the pole and a diameter that increases with increasing coil winding radius [8, 9]. Therefore, the PS of the light can reach a latitude on the Poincare sphere near its equator and, accordingly, acquire small ellipticity angles (up to $\varepsilon_{av} \approx 23°$ at the present parameters of the coil and an initial ellipticity angle of $45°$). As shown in Section 3.5, the ellipticity angle at the output end of the spun fibre (at the ends of the sensing coil) depends on the

length L_{res}, i.e. on the difference between the length of the spun fibre and an integer number of precession lengths, L_{pr} [see formula (14)]. Since L_{pr} is temperature-dependent (Section 3.4), so are the length L_{res} and, accordingly, the ellipticity angle of the light at the fibre output end (Section 3.5), ensuring a periodic temperature dependence of visibility, with a period given by (17).

At a coil radius of 95 mm, the PS evolves around the pole of the Poincare sphere, deviating from it by no more than $10°$. If the temperature varies, the associated variation in the precession length should also lead to variations in the length L_{res} and, hence, in the PS at the output end of the spun fibre. However, these temperature variations of the PS have essentially no effect on fringe visibility, because the indicated PS's have roughly the same ellipticity angle, near the maximum angle, at any point of the precession loop, and according to Section 3.1 [formula (8)] interferometer visibility depends only on this angle.

If the ambient temperature varies, the effect found in this study may give rise to errors in measurements with a fibre-optic current sensor having a small spun fibre-based sensing coil. As follows from the above, this destabilising factor can be minimised by taking measures in order to reduce the difference between the ellipticity angles of the PS of the light within a precession loop. There are, in principle, two possibilities for achieving this:

1. One can produce not circularly but elliptically polarised light at the input of the sensing coil, like in a previous study [10]. The estimate in Section 3.6 suggests that, in the case of the sensing coil used in our experiments, with a fibre bend radius $R = 14$ mm, the minimum effect will take place at a PS ellipticity angle of $\sim 32.4°$.

2. In the case of a small sensing coil, one can use spun fibre with a reduced temperature coefficient of BR, e.g. microstructured fibre [18].

5. Conclusions

We have experimentally demonstrated and investigated periodic oscillations of interferometer visibility in a current sensor in response to changes in the temperature of a small-radius spun fibre-based sensing coil. The observed effect has been shown to depend on the magnitude of the bend-induced linear BR in the spun fibre in the magnetically sensitive coil and the temperature behaviour of the built-in linear BR in the fibre. The effect has been interpreted in terms of the periodic character of PS evolution in spun fibre over the characteristic precession length L_{pr} and the temperature dependence of the precession length.

The observed temperature effect on interferometer visibility can cause errors in the response of a small-coil fibre-optic current sensor operating at a variable ambient temperature. We have formulated recommendations as to ways of minimising the influence of this effect on the accuracy of measurements with a current sensor.

References

1. Enokihara A., Isutsu M., Sueta T. *J. Lightwave Technol.*, **5**, 1584 (1987).
2. Laming R.I., Payne D.N. *J. Lightwave Technol.*, **7** (12), 2084 (1989).
3. Bohnert K., Gabus P., Nehring J., Brandle H. *J. Lightwave Technol.*, **20**, 267 (2002).

4. Gubin V.P., Isaev V.A., Morshnev S.K., Sazonov A.I., Starostin N.I., Chamorovskii Yu.K., Usov A.I. *Quantum Electron.*, **36** (3), 287 (2006) [*Kvantovaya Elektron.*, **36** (3), 287 (2006)].
5. Born M., Wolf E. *Principles of Optics* (Cambridge: Cambridge University Press, 2002).
6. Frosio G., Dändliker R. *Appl. Opt.*, **33** (25), 6111 (1994).
7. Morshnev S.K., Gubin V.P., Isaev V.A., Starostin N.I., Chamorovsky Yu.K. *Foton-Ekspress*, **6** (62), 167 (2007).
8. Morshnev S.K., Gubin V.P., Isaev V.A., Starostin N.I., Sazonov A.I., Chamorovsky Yu.K., Korotkov N.M. *Optical Memory and Neural Networks (Information Optics)*, **17** (4), 258 (2008).
9. Morshnev S.K., Gubin V.P., Vorob'ev I.L., Starostin N.I., Sazonov A.I., Chamorovsky Yu.K., Korotkov N.M. *Quantum Electron.*, **39** (3), 287 (2009) [*Kvantovaya Elektron.*, **39** (3), 287 (2009)].
10. Przhiyalkovsky Ya.V., Morshnev S.K., Starostin N.I., Gubin V.P. *Quantum Electron.*, **44** (10), 957 (2014) [*Kvantovaya Elektron.*, **44** (10), 957 (2014)].
11. Przhiyalkovsky Ya.V., Morshnev S.K., Starostin N.I., Gubin V.P. *Quantum Electron.*, **45** (11), 1075 (2015) [*Kvantovaya Elektron.*, **45** (11), 1075 (2015)].
12. Polinkin P., Blake J. *J. Lightwave Technol.*, **23**, 3815 (2005).
13. Azzam R.M.A., Bashara N.M. *Ellipsometry and Polarized Light* (Amsterdam–New York–Oxford: North-Holland Publishing Company, 1977).
14. Rashleigh S.C. *J. Lightwave Technol.*, **1** (2), 312 (1983).
15. Przhiyalkovsky Ya.V., Morshnev S.K., Starostin N.I., Gubin V.P. *Quantum Electron.*, **43** (2), 167 (2013) [*Kvantovaya Elektron.*, **43** (2), 167 (2013)].
16. Nekrashevich E.S., Ryabko M.V. *Nelineinyi Mir*, **5** (5), 292 (2007).
17. Shayne X.S., Tselikov A.A., de Arruda J.U., Blake J.N. *J. Lightwave Technol.*, **16** (7), 1222 (1998).
18. Mishie A., Canning J., Bassett I., et al. *Opt. Express*, **15**, 1811 (2007).